JMEPEG (2010) 19:434–450
DOI: 10.1007/s11665-009-9509-4

1059-9495/$19.00

Derivation, Parameterization and Validation of a Sandy-Clay Material Model for Use in Landmine Detonation Computational Analyses

M. Grujicic, B. Pandurangan, N. Coutris, B.A. Cheeseman, W.N. Roy, and R.R. Skaggs

(Submitted June 1, 2009)

A set of large-strain/high-deformation-rate/high-pressure material models for sand-based soils with different saturation levels and clay and gravel contents was recently proposed and validated in our study, and the same has been extended in this study to include clay-based soils of different saturation levels and sand contents. The model includes an equation of state which reveals the material response under hydrostatic pressure, a strength model which captures material elastic-plastic response under shear, and a failure model which defines the laws and conditions for the initiation and evolution of damage and ultimate failure of the material under negative pressure and/or shear. The model was first parameterized using various open-literature experimental results and property correlation analyses and, then, validated by comparing the computational results obtained in an ANSYS/Autodyn-based transient non-linear dynamics analysis of detonation of a landmine buried in sandy-clay with their experimental counterparts.

Keywords blast resistance, granular materials, material modeling

1. Introduction

It is nowadays widely recognized that, despite the signing of the Mine Ban Treaty in 1999, there is an ongoing landmine crisis. The main aspects of this crisis include (a) unexploded landmines in excess of 100 million remain deployed in over 60 countries all over the world (Ref 1); (b) nearly, 30,000 civilians are killed or maimed every year by unintended detonations of the mines (Ref 2); (c) the cost of medical treatment of landmine injuries exceed 100 million per year (Ref 3); (d) the ability of the international community to provide the humanitarian relief in terms of medical services, safe drinking water, food, etc., is greatly hampered by landmine contamination of the infrastructure in mine-affected countries (Ref 3), to name a few. In order to address the aforementioned landmine crisis, the research community around the world has taken upon itself the challenge of helping better understand the key phenomena associated with landmine detonation and interaction between detonation products, mine fragments, and soil ejecta with the targets (people, structures, and vehicles). Such improved understanding will help automotive manufacturers to design and fabricate personnel carriers with higher landmine-detonation survivability characteristics and a larger level of protection for the onboard personnel (Ref 4-7). In addition, the manufacturers of de-mining equipment and personnel protection gear used in landmine clearing are expected to benefit from a better understanding of the landmine detonation-related phenomena.

A review of the public-domain literature carried out as a part of this study revealed that the landmine detonation-related research activities can be broadly divided into three main categories: (a) shock and blast wave mechanics/dynamics including landmine detonation phenomena and large-deformation/high-deformation rate constitutive models for the attendant materials (high explosive, air, soil, etc.); (b) the kinematic and structural response of the target to blast loading including the role of target design and use of blast attenuation materials; (c) vulnerability of human beings to post-detonation phenomena such as high blast pressures, spall fragments, and large vertical and lateral accelerations. This study falls primarily into the category (a) of the research listed above since it emphasizes the development of a large-deformation/high-deformation-rate/high-pressure material model for clay-based soil at different saturation levels and sand contents. It is generally recognized that the properties of soil, into which a landmine is buried, play an important role in the overall effectiveness/lethality of the landmine regardless of the nature of its deployment (fully buried, flush-buried, or ground-laid). It should further be recognized that this study, primarily within its material-model validation stage, also addresses briefly the category (b) of the landmine detonation-related research.

While there are a variety of soils, it is customary to divide all the soils in two main categories: (a) *Cohesion-less soils* (e.g., sand) which consist of relatively coarse particles (average particle size 0.2-2 mm) which have a negligible tensile strength and derive their shear strength primarily from the inter-particle friction; (b) *Cohesive soils* (e.g., clay) which consist of fine particles (average particle size 10-50 μm) which derive their strength and failure properties from the inter- and intra-particle

M. Grujicic, B. Pandurangan, and **N. Coutris**, International Center for Automotive Research CU-ICAR, Department of Mechanical Engineering, Clemson University, Clemson, SC 29634; and **B.A. Cheeseman, W.N. Roy,** and **R.R. Skaggs**, Army Research Laboratory – Survivability Materials Branch, Aberdeen Proving Ground, MD 21005-5069. Contact e-mails: mica.grujicic@ces.clemson.edu and mica@ces.clemson.edu

electrostatic and polar forces. In this study, the problem of material model derivation and validation for clay-based soils at various saturation levels and sand contents is addressed (referred to as *the sandy-clay soil* or *sandy clay*, in the remainder of this manuscript).

A review of the open-domain literature carried out as a part of this study revealed that there exists an extensive body of study dealing with the investigation of the detonation of the buried charges. However, much of this study does not focus on the characterization of the blast output of landmines, but rather on cratering effects in soils, with applications toward the efficient utilization of explosives for excavation (i.e., canals, trenches, etc.) or in the survivability of structures subjected to near surface blasts (Ref 8). Westine et al. (Ref 9) carried out experiments on a plate which was mounted above a buried charge comparable is size and power to an anti-tank landmine. The plate contained a number of through-the-thickness holes at incremental distances from the mine, in which, plugs of known mass were placed. The blast accompanying mine detonation caused the plugs to be ejected from the holes, and from their initial velocity, the impulsive loading on the plate was calculated. Morris (Ref 10) used the results of Westine et al. (Ref 9) to construct a design-for-survivability computer code for lightweight vehicles. More recently, Bergeron et al. (Ref 11) carried out a comprehensive investigation of the buried landmine blasts using an instrumented ballistic pendulum. From these experiments, the pressure and impulse as a function of time were recorded at several locations in air directly above the mine as well as in the sand surrounding the landmine. In addition, x-ray radiography and high-speed photography were employed to investigate temporal evolution of the associated soil cratering and soil ejection phenomena.

In our recent computational study (Ref 12), based on the use of ANSYS/Autodyn, a general-purpose transient non-linear dynamics explicit simulation software (Ref 7), a detailed comparison was made between the experimental results of Bergeron et al. (Ref 13) and their computational counterparts for a number of detonation-related phenomena such as the temporal evolutions of the shape and size of the over-burden sand bubbles and of the detonation-products gas clouds, the temporal evolutions of the side-on pressures in the sand and in air, etc. It was found that the most critical factor hampering a better agreement between the experiment and computational analysis is an inadequacy of the current material model for sand to capture the dynamic response of this material under blast loading conditions. Hence, the main objective of our subsequent study was to improve the compaction material model proposed by Laine and Sandvik (Ref 14) implemented in ANSYS/Autodyn material database (Ref 7).

Soil is a very complicated material whose properties vary greatly with the presence/absence and relative amounts of various constituent materials (sand, clay, silt, gravel, etc.), as well as particle sizes and particle size distribution of the materials. In addition, the moisture content, and the extent of pre-compaction can profoundly affect the soil properties. The so-called "*porous-material/compaction*" model proposed by Laine and Sandvik (Ref 14) has been, for quite some time, the soil model which provided the best compromise between the inclusion of essential physical phenomena reflecting material response under dynamic loading and computational simplicity. However, this model was developed essentially for dry sand and, as demonstrated by many researchers (e.g., Ref 8, 11, 15), cannot account for the effects of moisture, clay and or gravel in soil. In order to overcome these deficiencies of the original porous-material/compaction model, Clemson University and the Army Research Laboratory (ARL), Aberdeen, Proving Ground, MD jointly developed (Ref 16) and subsequently parameterized (using the results of a detailed investigation of dynamic response of sand at different saturation levels, as carried out by researchers at the Cavendish Laboratory, Cambridge, UK; Ref 17, 18) the new sand model (Ref 19). This model was shown to be capable of capturing the effect of moisture on the dynamic behavior of sand and was named *the CU-ARL sand model*. In a subsequent study (Ref 5), Clemson University and the ARL developed the so-called *CU-ARL clayey sand model* to include the effect of minor (<15 vol.%) additions of clay on the dynamic mechanical response of sand. In the latest publically reported soil material-model development effort by Clemson University and the ARL, the effect of gravel in sand was accounted for (to comply with the STANAG 4569 material-model requirements; Ref 20) and the resulting soil material model named the *CU-ARL sandy gravel* model (Ref 6).

In this study, the aforementioned set of the CU-ARL material models for different types of soils is expanded to include the case of clay-based soils at different levels of saturation and various sand contents. Since this model was jointly developed by Clemson University and the ARL, it will be referred to, in the remainder of the document, as the *CU-ARL sandy-clay soil model*. As will be shown in the next section, the dynamic mechanical response of sandy-clay soils is significantly different from that of sand-based soils due to the interplay of a number of physico-chemical phenomena such as electrostatic bonding-enhanced inter-particle adhesion in clay, osmosis-based tendency of clay to absorb and retain water, water-absorption-induced swelling of clay, etc. It should also be noted that in our previous study (Ref 5), a material model for sand-based soil containing less than ca. 15 vol.% clay (CU-ARL clayey sand model) was developed, while the model discussed in this study (the CU-ARL sandy-clay model) pertains to the clay-based soil containing minor additions of sand. A comparison of the basic architecture of the two types of soil is displayed in Fig. 1(a) and (b). In the case of clayey sand, displayed in Fig. 1(a), coarser sand particles are coated with a layer of clay while in the case of sandy-clay, Fig. 1(b), fine clay particles form a continuous matrix within which discrete sand particles are dispersed. In should be also noted that the terms "*sandy clay*" and "*clay-based soils*" have been used interchangeably throughout this article.

The organization of this article is as follows. Morphology and microstructure of sand and clay at the atomic and particle/aggregate length scales are compared and contrasted in Sect 2.1 and 2.2, respectively. The effect of the identified morphological/microstructural differences on the differences in dynamic mechanical response of the two types of soils is discussed in Sect 2.3. Derivation and parameterization of the CU-ARL sandy-clay material model are discussed in Sect 2.4. The results of the model validation via comparison of the computational and experimental results for a number of scenarios involving landmine detonation in sand and clay and subsequent interactions of the detonation products, mine fragments, and soil ejecta are presented and discussed in Sect 3. A brief summary and the conclusions obtained in this study are discussed in Sect 4.

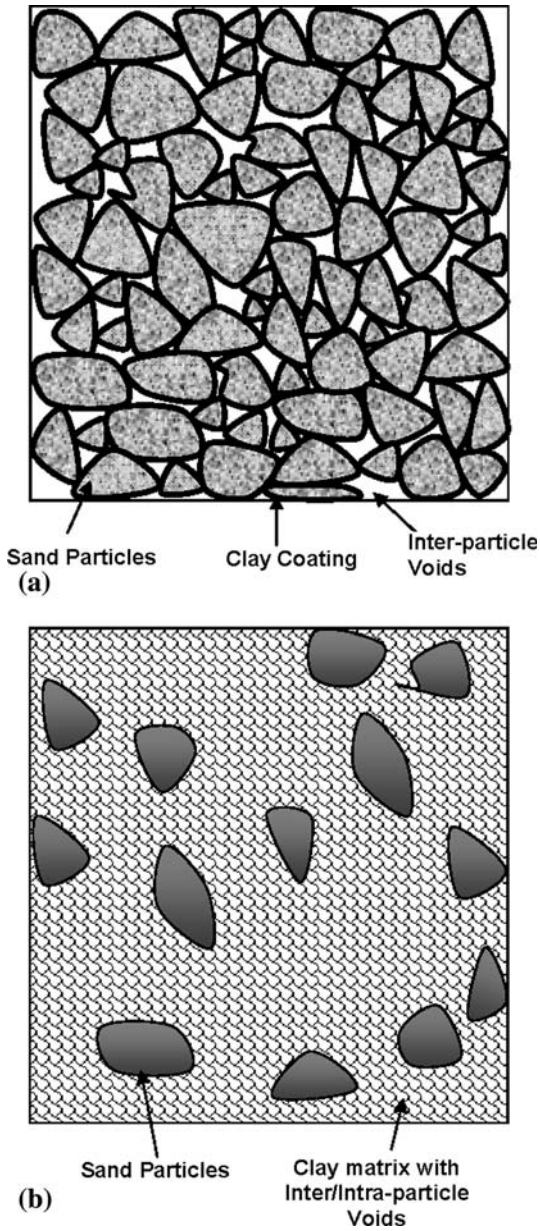

Fig. 1 Basic morphology of: (a) the Cu-ARL clayey sand and (b) the CU-ARL sandy clay

2. Model Derivation and Computational Analysis

2.1 Atomic-Level Microstructure and Morphology of Sand and Clay

As stated earlier, soils are generally classified into two groups: (a) those dominated by sand and (b) those consisting of major fractions of clay. While in both cases, the basic architecture of soil involves a skeleton of solid particles and interconnected spaces (voids) filled with air and/or water, significant differences exist in the microstructure of the two types of soil both at the atomic length-scale and the particle/aggregate-length scale. Among these differences, the most important ones are outlined in this and the following section.

In most cases, sand is based on silicon-dioxide (SiO_2). At the atomic length-scale, sand consists of silica-tetrahedrons

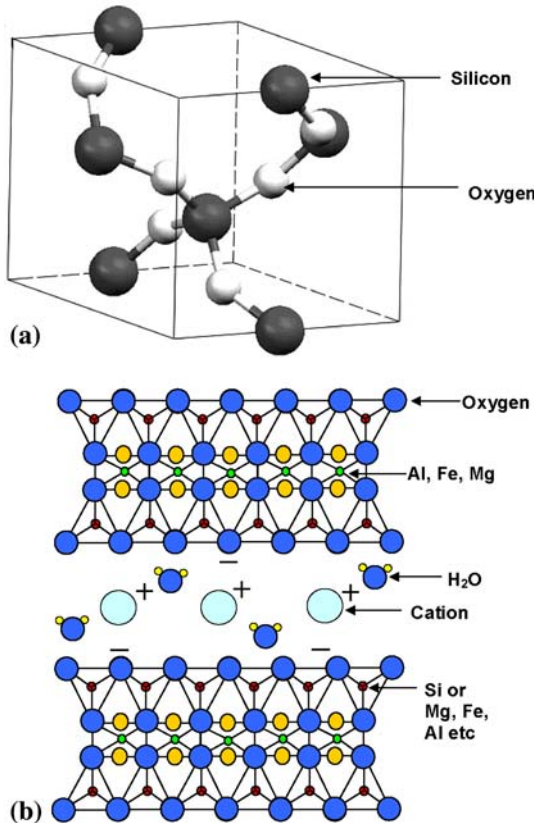

Fig. 2 A schematic of the atomic-level microstructure of: (a) α-quartz and (b) clay

(SiO_4^{4-}) typically arranged in the form of a quartz allotropic modification, Fig. 2(a). Due to the covalent nature of its inter-atomic bonding and its compacted atomic microstructure, quartz behaves as an inert and quite hard material. Consequently, no water absorption by quartz takes place and no significant sand inter-particle adhesion exists.

In sharp contrast, the atomic-level microstructure of clay, as displayed in Fig. 2(b), reveals that this material is composed of sheet-like silicate layers with a particular stacking sequence. In natural clay, this sequence involves a central layer consisting mainly of aluminum cations (and oxygen anions) sandwiched between two tetrahedral layers consisting of silicon cations and oxygen anions. Typically, some of the aluminum and silicon ions are replaced by lower valence ions such as Mg^{2+}, Ca^{2+}, Li^{+}, etc., creating a negative charge imbalance in each of the three-layer sheets. The charge imbalance is neutralized by adsorption of Na^{+}, Ca^{2+}, and K^{+} cations which tend to have water molecules associated with them. The hydrated Na^{+}, Ca^{2+}, and K^{+} cations residing in the interlayer region make clay behave as a pliable material and, at higher water levels, cause the clay to swell.

2.2 Particle/Aggregate-Level Microstructure of Sand and Clay

As stated in the previous section, the basic architecture of both sand and clay involves a skeleton of contacting particles and/or aggregates of particles separated by pores/voids. However, the particle/aggregate microstructure of the two types of soils is different in at least two major aspects: (a) sand particles

are typically coarse (average particle size ca. 0.2-2 mm), homogeneous, quite rigid and brittle while, clay particles are finer (average particle size ca. 10-50 μm) and contain stacks of three-layer sheets, are pliable and ductile; and (b) while air and water may reside in the inter-particle spaces in the case of both sand and clay, intra-particle moisture (moisture residing in the spaces separating adjacent sheets) is present exclusively in clay making it pliable and ductile even in an unsaturated condition. Also, it is the intra-particle water that is believed to be primarily responsible for clay swelling observed at larger saturation levels. This finding is commonly explained as follows: In unsaturated clay, the exchangeable inter-layer cations are located on the surface of the layers or in the hexagonal holes of the tetrahedral sheets. In this state, the adjacent clay layers lie so close to each other that they are almost in contact. That is, the inter-layer distances are quite small (approximately 1 nm) and, hence, the negatively charged layers are held together very strongly to the inter-layer cations via ionic and van der Waals forces. After their hydration, the cations tend to position themselves half-way between the clay layers, and this leads to the widening of spaces between the layers, i.e., to the swelling of clay. In sharp contrast, since water absorption into inter-particle spaces is mainly a physical phenomena based on capillary effects, sand swelling caused by water absorption is typically not significant.

The removal of intra-particle water generally requires drying/baking of clay resulting in a hard and brittle material containing multiple shrinkage-induced cracks. The behavior of dried/baked clay is not generally relevant in the computational analysis of a landmine detonation and is not considered in this study.

2.3 The Effect of Sand/Clay Microstructure on Their Mechanical Behavior

Considering the aforementioned differences in the microstructure of sand and clay at the atomic and particle/aggregate length scales, one may anticipate differences in the behavior of these two types of soil when subjected to static and dynamic loading conditions. Among these differences, the main ones can be summarized as follows:

(a) In the case of sand, the strength is controlled by inter-particle friction and, hence, generally increases with an increase in confining pressure, till the point of full compaction. While the presence of moisture in sand reduces the magnitude of the inter-particle friction coefficient, the strength remains dependent on the magnitude of confining pressure as the saturation-level is increased (Ref 4). In sharp contrast, the magnitude of the inter-particle friction coefficient of clay is generally found to be only weakly affected by the magnitude of confining pressure (Ref 21), while the saturation level still affects the magnitude of the strength of clay. The latter findings are explained as follows: Due to the relatively tight bonding of the intra-particle water, this water is quite immobile, causing the effective pore pressure to remain essentially constant as the confining pressure is increased. This, in turn causes the strength of clay to be controlled by the shear strength of the intra-particle water bonded layers and thus to be less affected by the magnitude of confining pressure. As far as the effect of intra-particle water on clay strength is concerned, it is believed to be associated with the fact that the water molecules tend to orient their negative poles toward positively charged cations and the resulting shielding effect reduces the electrostatic attraction between the negatively charged clay layers and the positively charged inter-layer cations. Consequently, while moisture reduces the strength in both sand and clay, this effect is significantly more pronounced in the case of clay (Ref 21);

(b) Inter-particle cohesion in sand generally increases with an increase in the level of saturation which is attributed to the capillary affects associated with inter-particle voids. In sharp contrast, cohesive strength of clay is generally decreased as the level of saturation is increased, which is attributed to the intra-particle water absorption that leads to an increase in the inter-layer separation and a reduction of the inter-layer bonding strength;

(c) Stress-rate sensitivity of the deformation behavior of sand and clay at different levels of saturation is also quite different. That is, the deformation of sand is generally believed to involve two main basic mechanisms (Ref 22-24): (a) elastic deformations (at low pressure levels) and fracture (at high pressure levels) of the inter-particle bonds and (b) elastic and plastic deformations of the three constituent materials in the sand (sand particles, air, and water). The relative contributions of these two deformation mechanisms as well as their behavior are affected primarily by the degree of saturation of sand and the deformation rate. Specifically, in dry sand, the first mechanism controls the sand deformation at low pressures, while the second mechanism is dominant at high pressures and the effect of deformation rate is of a second order. In sharp contrast, in saturated sand, very low inter-particle friction diminishes the role of the first deformation mechanism. On the other hand, the rate of deformation plays an important role. At low deformation rates, the water/air residing in the sand pores is squeezed out during deformation and, consequently, the deformation of the sand is controlled by the deformation of the solid mineral particles. At high pressures, on the other hand, water/air is trapped within the sand pores and the deformation of the sand is controlled by the deformation and the volume fractions of each of the three constituent phases.

The dynamic mechanical behavior of clay, on the other hand, is significantly less sensitive to the rate of deformation at any level of saturation. This behavior of clay is attributed to its ability to easily absorb and retain water within its intra-particles spaces. In other words, while at low deformation-rate conditions, the inter-particle water in clay can still be squeezed out, the intra-particle water is retained giving rise to a low value of compressibility of the clay (similar to that observed at high deformation-rates).

2.4 Material Model Development for Sandy Clay

As discussed earlier, the main objective of this study is to derive a material for clay-based soils with various levels of sand content and water saturation. This model is needed and will be used in the computational analyses of various landmine-detonation scenarios involving various types of deployments in the clay-rich soil. Since the computational analyses in question are of a transient, non-linear dynamic nature, the clay-based soil material model to be developed (*the CU-ARL sandy clay model*)

is primarily aimed at the response of this material under large deformation, high-deformation rate, and large pressure conditions. The validity of the model under slow-speed quasi-static conditions (e.g., the loading conditions encountered during tire/soil interactions) is not the subject of this study.

As discussed in our previous study (Ref 4-6), a typical transient non-linear dynamics problem involves numerical solution of the governing mass, momentum, and energy conservation equations. Spatial coordinates and time are independent variables while mass density, velocities, and the internal energy densities are the dependent variables in these equations. Since the stress appears explicitly in these equations, a set of relations (the material model) is needed to establish (for a given material) the relationships between stress and the dependent variables (and/or there integrals). Furthermore, since stress, σ, is generally decomposed into a hydrostatic stress ($-pI$, where p is the pressure and I is a second-order identity tensor), and a deviatoric stress, σ_d, the material model is generally decomposed into:

(a) An *Equation of State*, EOS (defines the density and internal energy density dependences of pressure);

(b) A *strength model* (used to express the evolution of deviatoric stress in the elastic and elastic-plastic region of the material) and

(c) A *failure model* (defines the damage/failure response of the material).

In addition to these relations, an erosion model is often defined to alleviate numerical difficulties arising in regions experiencing large deformations. Within the erosion model, heavily deformed regions can be removed while conserving their momenta via the retention of the associated nodes as well as the nodal masses and velocities. In the remainder of this section, a brief overview is presented of the derivation of an equation of state, a strength model, a failure model, and an erosion model for sandy clay.

Since the CU-ARL sandy clay material model developed in this study is intended to include the effects of porosity, inter-particle water saturation content, and sand content, the following parameters are defined to represent the physical and chemical states of the soil:

$$\alpha = \frac{V_{water} + V_{air}}{V_{total}} \quad \text{(Eq 1)}$$

$$\beta = \frac{V_{water}}{V_{water} + V_{air}} \quad \text{(Eq 2)}$$

and

$$\Omega = \frac{V_{sand}}{V_{clay} + V_{sand}} \quad \text{(Eq 3)}$$

where α is the extent of porosity, β the degree of saturation, Ω the solid fraction of sand (sand content), V is volume, and the subscripts *sand*, *clay*, *air*, *water*, and *total* are self explanatory.

2.4.1 CU-ARL Sandy-Clay Equation of State. In this section, the equation of state (EOS) representing the compaction behavior of sandy clay under hydrostatic pressure is presented. The EOS for the CU-ARL sandy clay is derived below following the same procedure which was originally employed to derive the CU-ARL sand EOS. That is the EOS is first separately derived for dry and fully saturated clay containing minor additions (<10 vol.%) of sand. These are next combined (using a simple rule of mixture) to define the corresponding relationships for unsaturated sandy clay. It is also recognized that clay and sand compaction behavior differ in at least two significant respects: (a) Clay particles are finer and can more readily be displaced under the soil's own weight to yield a lower level of initial porosity in the soil; (b) Clay particles are deformable which greatly facilitates the compaction of the clay-based soil while, in sharp contrast, in sand-based soils, sand-particle fracture is generally required for soil compaction.

Dry Sandy Clay: The relevant CU-ARL dry sandy clay EOS relations are presented first. Following our previous study (Ref 4-6), the dry-clay pressure dependence on mass density is defined using the following three-part piece-wise linear relation:

$$P_{dryclay} = \begin{cases} 0 & \rho_{dryclay} \le \rho_{o,dryclay} \\ B_{Pl.Comp,dryclay}\left(\rho_{dryclay} - \rho_{o,dryclay}\right) & \rho_{o,dryclay} \le \rho_{dryclay} \le \rho^*_{dryclay} \\ B_{El.Compr,dryclay}\left(\rho_{dryclay} - \rho_{s,dryclay}\right) & \rho_{dryclay} > \rho^*_{dryclay} \end{cases} \quad \text{(Eq 4)}$$

where $B_{Pl.Comp,dryclay}$ and $B_{El.Compr,dryclay}$ (= 12.11 MPa m^3/kg; Ref 25) are respectively the plastic compaction and the elastic compression moduli, while $\rho_{0,dryclay} = (1-\alpha_0)\rho_{s,dryclay}$ and $\rho_{s,dryclay}$ (= 2005 kg/m^3; Ref 26) are the initial zero-pressure density of dry clay and the density of the fully-compacted clay, respectively, and α_0 denotes the initial porosity in clay. It should be noted, that the compaction and elastic-compression moduli used in Eq 4 are defined as a ratio of the corresponding bulk moduli and mass densities. The plastic compaction modulus, $B_{Pl.Comp,dryclay}$, is defined as:

$$B_{Pl.Comp,dryclay} = \frac{P_{Comp,dryclay}}{\left(\rho^*_{dryclay} - \rho_{0,dryclay}\right)} \quad \text{(Eq 5)}$$

where $P_{Comp,dryclay}$ (= ca. 0.1 GPa; Ref 27) is the minimum pressure needed for full densification of dry clay, and the corresponding mass density $\rho^*_{dryclay}$ is given by

$$\rho^*_{dryclay} = \rho_{s,dryclay} + \frac{P_{Comp,dryclay}}{B_{El.Compr,dryclay}} \quad \text{(Eq 6)}$$

In order to account for the effect of sand in dry clay (specifically for the fact that the compressibility of sand particles is small in comparison to that of clay particles), the CU-ARL dry clay EOS model parameters are next generalized as follows:

$$\begin{aligned} \rho_{0,drySandyclay} &= (1-\alpha_0)\rho_{s,drySandyclay} \\ &= (1-\alpha_0)\left[(1-\Omega)\rho_{s,dryclay} + \Omega\rho_{s,sand}\right] \end{aligned} \quad \text{(Eq 7)}$$

$$P_{Comp,drySandyclay} = (1-\Omega)P_{Comp,dryclay} + \Omega P_{Comp,sand} \quad \text{(Eq 8)}$$

$$B_{Pl.Comp,drySandyclay} = \frac{P_{Comp,drySandyclay}}{\left(\rho^*_{drySandyclay} - \rho_{0,drySandyclay}\right)} \quad \text{(Eq 9)}$$

$$\rho^{*}_{\text{drySandyclay}} = \rho_{\text{s,drySandyclay}} + \frac{P_{\text{Comp,drySandyclay}}}{B_{\text{El.Compr,drySandyclay}}} \quad \text{(Eq 10)}$$

and

$$B_{\text{El.Compr,drySandyclay}} = (1-\Omega)B_{\text{El.Compr,dryclay}} + \Omega B_{\text{El.Compr,sand}} \quad \text{(Eq 11)}$$

Saturated Sandy Clay: In ordet to account for the fact that under high deformation-rate conditions, intra- and inter-particle waters are trapped within the soil (which prevents significant plastic compaction of soil), and the EOS for saturated clay-based soil is defined using the following two-part piece-wise linear function:

$$P_{\text{satSandyclay}} = \begin{cases} 0 & \rho_{\text{satSandyclay}} \le \rho_{0,\text{satSandyclay}} \\ B_{\text{satSandyclay}}\left(\rho_{\text{satSandyclay}} - \rho_{0,\text{satSandyclay}}\right) & \rho_{\text{satSandyclay}} > \rho_{0,\text{satSandyclay}} \end{cases} \quad \text{(Eq 12)}$$

where $B_{\text{satSandyclay}}$ is the compaction modulus of saturated sandy clay and is defined using the elastic compression modulus of dry sandy clay, $B_{\text{El.Compr,drySandyclay}}$ and the compaction modulus of water, B_{w}, and the fact that both the solid phase and the water-filled porosity form continuous networks, as

$$\gamma_1 = \beta\left[\frac{1 - \frac{P_{\text{Comp,dry,Sandyclay}}}{B_{\text{satSandyclay}}\rho^{*}_{\text{satSandyclay}}}}{(1-\beta)\left(1 - \frac{P_{\text{Comp,drySandyclay}}}{B_{\text{Pl.Comp,drySandyclay}}\rho^{*}_{\text{drySandyclay}}}\right) + \beta\left(1 - \frac{P_{\text{Comp,drySandyclay}}}{B_{\text{satSandyclay}}\rho^{*}_{\text{satSandyclay}}}\right)}\right] \quad \text{(Eq 20)}$$

$$B_{\text{satSandyclay}} = (1-\alpha_0)B_{\text{El.Compr,drySandyclay}} + \alpha_0 B_{\text{w}} \quad \text{(Eq 13)}$$

while $\rho_{0,\text{satSandyclay}}$ is the initial density of saturated sandy clay and is defined in terms of the density of dry sandy clay, $\rho_{\text{s,drySandyclay}}$, and the density of water, ρ_{w}, as

$$\rho_{0,\text{satSandyclay}} = (1-\alpha)\rho_{\text{s,drySandyclay}} + \alpha\rho_{\text{w}} \quad \text{(Eq 14)}$$

Unsaturated Sandy Clay: The pressure versus density curve for unsaturated sandy clay is obtained as a linear combination of the pressure versus density relations for the dry sandy and the saturated sandy clay, as:

$$P_{\text{unsat,Sandyclay}}(\alpha_0,\beta,\Omega) = \begin{cases} 0 & \rho_{\text{unsat,Sandyclay}} \le \rho_{0,\text{unsat,Sandyclay}} \\ B_{\text{unsat,Sandyclay,low}}\left(\rho_{\text{unsat,Sandyclay}} - \rho_{0,\text{unsat,Sandyclay}}\right) & \rho_{0,\text{unsat,Sandyclay}} \le \rho_{\text{unsat,Sandyclay}} \le \rho^{*}_{\text{unsat,Sandyclay}} \\ B_{\text{unsat,Sandyclay,high}}\left(\rho_{\text{unsat,Sandyclay}} - \rho^{*}_{\text{unsat,Sandyclay}}\right) & \rho_{\text{unsat,Sandyclay}} > \rho^{*}_{\text{unsat,Sandyclay}} \end{cases} \quad \text{(Eq 15)}$$

$$K_{\text{dryclay}} = \begin{cases} 0 & \rho_{\text{dryclay}} < \rho_{0,\text{dryclay}} \\ -22.01 + 0.01565\rho_{\text{dryclay}} & \rho_{0,\text{dryclay}} < \rho_{\text{dryclay}} \le 0.8407\rho_{\text{s,dryclay}} \\ -119.93 + 0.07358\rho_{\text{dryclay}} & 0.8407\rho_{\text{s,dryclay}} \le \rho_{\text{dryclay}} \le 0.9714\rho_{\text{s,dryclay}} \\ -979.94 + 0.5152\rho_{\text{dryclay}} & 0.9714\rho_{\text{s,dryclay}} < \rho_{\text{dryclay}} < \rho_{\text{s,dryclay}} \\ -4.4088 + 0.0306\rho_{\text{dryclay}} & \rho_{\text{dryclay}} > \rho_{\text{s,dryclay}} \end{cases} \quad \text{(Eq 21)}$$

where

$$\rho_{0,\text{unsat,Sandyclay}} = (1-\beta)\rho_{0,\text{drySandyclay}} + \beta\rho_{0,\text{satSandyclay}} \quad \text{(Eq 16)}$$

$$\rho^{*}_{\text{unsat,Sandyclay}} = (1-\gamma_1)\rho^{*}_{\text{drySandyclay}} + \gamma_1\rho^{*}_{\text{satSandyclay}} \quad \text{(Eq 17)}$$

$$B_{\text{unsat,Sandyclay,low}} = \frac{P_{\text{Comp,drySandyclay}}}{\left(\rho^{*}_{\text{unsat,Sandyclay}} - \rho_{0,\text{unsat,Sandyclay}}\right)} \quad \text{(Eq 18)}$$

and

$$B_{\text{unsat,Sandyclay,high}} = \left[\frac{1}{\frac{(1-\beta)}{B_{\text{El.Compr,drySandyclay}}} + \frac{\beta}{B_{\text{satSandyclay}}}}\right] \quad \text{(Eq 19)}$$

where

Equation 19 reflects the fact that the compaction modulus of the material residing in the intra- and inter-particle voids in sandy clay, consisting of dry air and water, is dominated by its more compliant phase (dry air).

Equation 8-20 define the pressure versus density relation during loading which results in (irreversible) compaction of sandy clay. During unloading/elastic-reloading the pressure versus density relationship is nearly linear with the slope being equal to the square of the (density-dependent) sound speed, C. Thus, in order to fully define the CU-ARL sandy clay EOS model, a C versus ρ relation must also be specified. The material sound speed is defined as the square-root of the ratio of the bulk modulus and the material mass density.

Dry Sandy Clay: The bulk modulus (in GPa) versus density relationship for dry clay is given as (Ref 5):

In order to account for the effect of sand in CU-ARL dry sandy clay, the dry clay bulk modulus K_{dryclay} given by Eq 21 is modified as

$$K_{\text{drySandyclay}} = \left[\frac{1}{\frac{(1-\Omega)}{K_{\text{dryclay}}\left(\rho_{\text{dryclay}}\right)} + \frac{\Omega}{K_{\text{sand}}}}\right] \quad \text{(Eq 22)}$$

where K_{sand} is the bulk modulus of solid-sand particles (= 21.97 GPa; Ref 26).

Saturated Sandy Clay: The density-dependent bulk modulus in saturated sandy clay is derived following the same procedure as in the case of P versus ρ relation as:

$$K_{\text{satSandyclay}} = B_{\text{satSandyclay}}\rho_{\text{satSandyclay}} \quad \text{(Eq 23)}$$

Unsaturated Sandy Clay: In the same way, the density-dependent bulk modulus for unsaturated sandy clay is defined as:

$$K_{\text{unsat,Sandyclay}}\left(\rho_{\text{unsat,Sandyclay}}, \Omega, \alpha_0, \beta\right) = \left[(1-\beta)K_{\text{drySandyclay}} + \beta K_{\text{satSandyclay}}\right] \quad \text{(Eq 24)}$$

where

$$\rho_{\text{drySandyclay}} = \rho_{\text{unsat,Sandyclay}} - \alpha_0\beta\rho_{\text{water}} \quad \text{(Eq 25)}$$

and

$$\rho_{\text{satSandyclay}} = \rho_{\text{unsat,Sandyclay}} + \alpha_0(1-\beta)\rho_{\text{water}} \quad \text{(Eq 26)}$$

The effects of (0, 50, and 100%) saturation on the P versus ρ and C versus ρ EOS relations in sandy clay with 10 vol.% sand are displayed in Fig. 3(a) and (b), respectively.

2.4.2 CU-ARL Sandy-Clay Strength Model. As discussed in Sect 2.3, the yield strength (σ_y) of clay is not significantly affected by the magnitude of confining pressure, and to the first order of approximation, can be represented using a pressure-independent ideal-plastic constitutive law. The pressure-invariant yield stress is, however, a decreasing function of the degree of saturation, and is assumed to vary linearly between its dry clay value (ca. 50 kPa; Ref 21) and its saturated-clay value (ca. 0.5 kPa; Ref 21). Minor additions of sand to the clay are modeled as the effect of rigid inclusions within a clay matrix. This effect is accounted for using a simple approach within which the yield strength of sandy clay, at any level of saturation, is obtained by multiplying the corresponding value for clay with a factor $1/(1-\Omega)$ (Ref 5).

In addition to specifying the yield stress versus pressure relationship, the strength model entails the knowledge of the shear modulus and its dependence on density and/or pressure. The shear modulus is used to define the relationship between the deviatoric stress and the deviatoric strain components during unloading/elastic reloading.

It is generally found that the shear modulus of dry clay is fairly independent of pressure, but it increases as mass density is increased. This increase is initially small and becomes larger and larger as the condition for full compaction is being reached. Once the full compaction condition is reached, shear modulus becomes essentially density independent. In order to account for this behavior, the following density-dependent relation for shear modulus of dry clay is proposed:

$$\begin{aligned} G_{\text{dryclay}} &= G^0_{\text{dryclay}} + G^1_{\text{dryclay}}\left(\rho_{\text{dryclay}} - \rho_{0,\text{dryclay}}\right)^n, \quad \rho_{\text{dryclay}} \le \rho_{\text{s,dryclay}} \\ G_{\text{dryclay}} &= G^0_{\text{dryclay}} + G^1_{\text{dryclay}}\left(\rho_{\text{s,dryclay}} - \rho_{0,\text{dryclay}}\right)^n, \quad \rho_{\text{dryclay}} > \rho_{\text{s,dryclay}} \end{aligned} \quad \text{(Eq 27)}$$

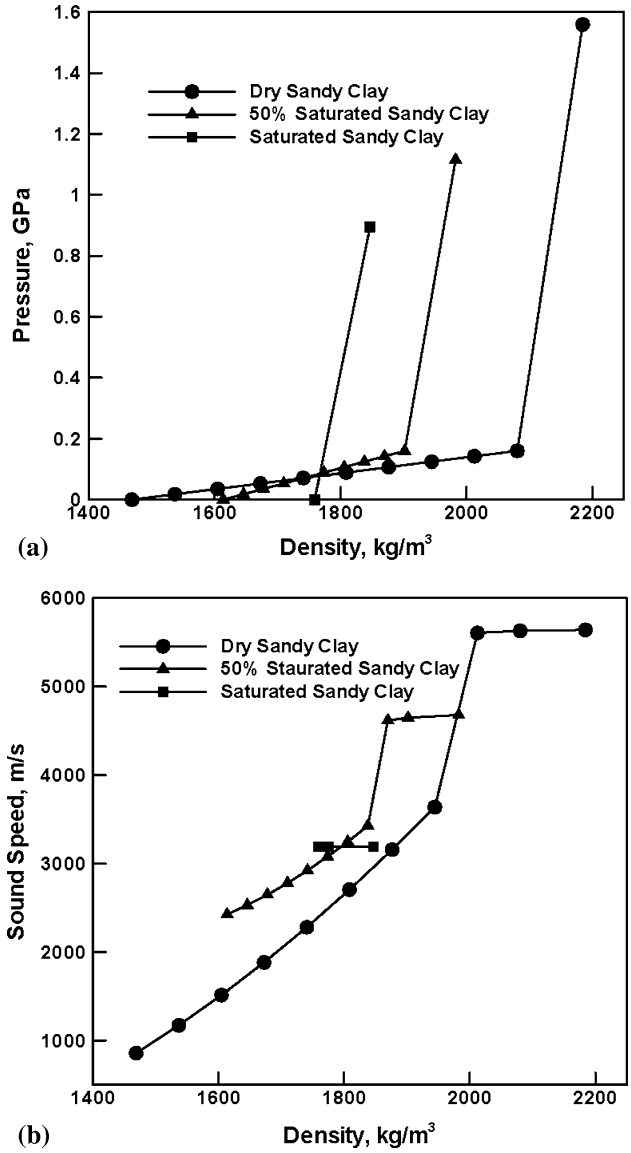

Fig. 3 (a) Pressure vs. density and (b) sound speed vs. density relation for dry, unsaturated and saturated CU-ARL sandy clay (10 vol.% sand) at different degrees of saturation

where G^0_{dryclay}(= ca. 0.9 GPa; Ref 28), G^1_{dryclay} (= 6.18×10^{-9} GPa; Ref 28), and n (= ca. 3; Ref 29) are the initial shear modulus, a shear modulus parameter, and a shear modulus exponent, respectively.

Since water has a negligibly small value of shear modulus, the effect of the degree of saturation on shear modulus in saturated and unsaturated clay is defined simply as

$$G_{\text{unsaturated,clay}} = G_{\text{saturatedclay}} + (1-\beta)\left(G_{\text{dryclay}} - G_{\text{saturatedclay}}\right) \quad \text{(Eq 28)}$$

where $G_{\text{saturatedclay}}$ is the shear modulus of fully saturated clay (= ca. 0.12 GPa; Ref 30).

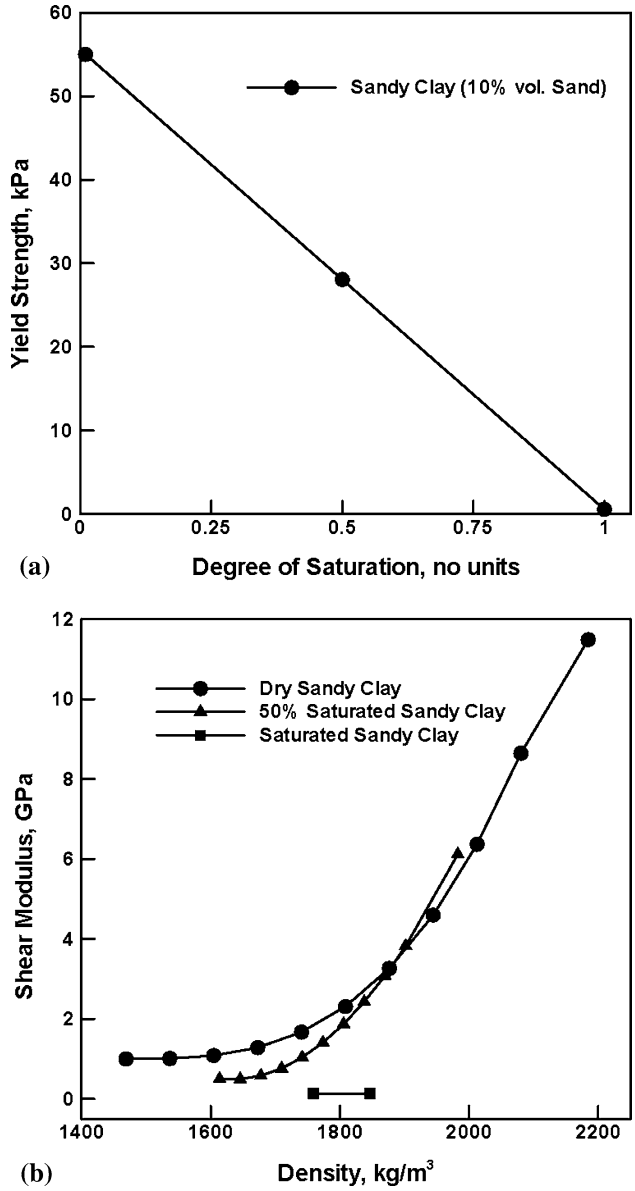

Fig. 4 (a) Yield stress vs. degree of saturation and (b) shear modulus vs. density relation for dry, unsaturated and saturated CU-ARL sandy clay (10 vol.% sand)

As in the case of yield strength, minor additions of sand cause elastic stiffening of clay and, hence, the shear modulus of sandy clay is obtained by multiplying the corresponding value for shear modulus for clay by a factor $(1/1 - \Omega)$.

The effects of saturation on σ_y and on the G versus ρ strength relation in sandy clay with 10 vol.% sand is displayed in Fig. 4(a) and (b), respectively.

2.4.3 CU-ARL Sandy-Clay Failure Model. In the suite of CU-ARL failure models for sand-based soils developed in our previous study (Ref 4-6), failure was assumed to occur when the negative pressure falls below a critical value, $P_{sand,fail}$ (i.e., a "*hydro*" type failure mechanism was adopted). After failure, the failed material element loses the ability to support tensile or shear loads while its ability to support compressive loads is retained. In dry sand-based soils, $P_{sand,fail}$ was set to $P_{drysand,fail} = 0$ (Ref 7). In saturated sand-based soils, on the other hand, capillary-induced inter-particle cohesion causes the failure pressure to acquire a more negative value ($= P_{saturatedsand,fail} = -70$ kPa; Ref 31). Furthermore, to account for the experimentally observed fact that the failure pressure in sand-based soils at the saturation level of 0.75 is around 15% of that in saturated sand (P_{fail}) (Ref 31), the following saturation-level dependent failure-pressure relation for unsaturated sand-based soils was proposed (Ref 4):

$$P_{unsatclayeysand,fail} = \beta^5 P_{fail.sat} \quad \text{(Eq 29)}$$

The CU-ARL failure models for the sand-based soils presented above were developed in Ref 4-6 to account for the fact that failure in these soils primarily takes place by negative-pressure-induced decohesion. In clay-based soils which are the subject of this study, on the other hand, it is generally observed that failure can occur not only due to decohesion but also due to excessive shearing. Hence, a hybrid ("*hydro*" + "*shear*") failure model will be developed below for the clay-based soils. In addition, the hybrid failure model will account for the fact that, while in sand-based soils increased saturation leads to an increase in the failure resistance of the soil, the cohesion strength in clay-based soils initially sharply increases (from its dry-soil value of ca. 60 kPa) with an increase in saturation until a peak value of ca. 225 kPa (Ref 32) (at a saturation level of ~40-50%) is attained, and then sharply decreases to a value of ca. 10 kPa in fully saturated clay (Ref 33).

The "*hydro*" portion of the failure model is considered first. In dry clay-based soils, intra- and inter-particle cohesion gives rise to a non-zero value of the negative failure pressure, $P_{dryclay,fail}$ (ca. −60 kPa; Ref 33). In saturated clay-based soils, the cohesion strength is greatly deteriorated and the $P_{saturatedclay,fail}$ becomes substantially less negative (ca. −10 kPa; Ref 33).

In order to account for the aforementioned effect of saturation on the cohesion strength of the unsaturated clay-based soils, $P_{unsaturatedclay,fail}$ is assumed to vary in accordance with the following relation with the degree of saturation as:

$$P_{unsaturatedclay,fail} = P_{dryclay,fail} - 720.8\beta + 770.8\beta^2 \quad \text{(Eq 30)}$$

The effect of sand particles in the clay-based soils on the cohesion-strength of these soils is not well understood (Ref 21). More evidence in the literature points out toward the fact that clay/sand particle interfaces are most likely places for decohesion-induced failure and, hence, the presence of sand compromises the ability of clay-based soils to withstand negative pressures. However, based on the results of prior studies, this effect does not appear to be major and, given the lack of required quantitative data, will not be taken into account in the present rendition of the CU-ARL sandy-clay material model. Hence, Eq 30 will be used in the "hydro" portion of the failure model of the sandy-clay soil under consideration.

Next, the shear-induced clay-based soil failure is considered. Failure is assumed to take place when the maximum shear stress reaches a critical level of saturation-level dependent shear-failure strength of the material. Increased saturation of the soil reduces the shear-failure strength of the soil, and this reduction scales nearly linearly with the extent of saturation (Ref 34). Hence, the shear-based portion of the failure model can be defined as

$$\tau_{unsaturatedclay,fail} = \tau_{dryclay,fail} + \beta\left(\tau_{saturatedclay,fail} - \tau_{dryclay,fail}\right) \quad \text{(Eq 31)}$$

where $\tau_{dryclay,fail}$ (= ca. 50 kPa; Ref 35) and $\tau_{saturatedclay,fail}$ (= ca. 20 kPa; Ref 35) are the dry and the saturated clay shear failure strengths, respectively.

Since sand particles hamper shear in clay-based soils, they generally have a significant effect on the ability of the clay-based soils to withstand shear without failure. In order to account for this effect, a simple non-deformable inclusion-based hardening model is adopted according to which the failure strength of clay-based soils (at any level of saturation) is defined by multiplying Eq 31 with a factor $(1/1 - \Omega)$.

It should be noted that within the current hybrid failure model for clay-based soils, interactions between the hydro and the shear modes of failure is not considered. In other words, failure occurs when conditions for either of the two failure mechanisms are met.

The effects of saturation on P_{fail} and τ_{fail} in sandy clay with 10 vol.% sand are displayed in Fig. 5(a) and (b), respectively.

2.4.4 CU-ARL Sandy-Clay Erosion Model. Erosion of highly distorted sandy-clay finite elements/cells is assumed to take place when the equivalent geometrical (i.e., elastic plus plastic plus damage/crack) instantaneous strain reaches a maximum allowable value. Our prior investigation (Ref 4-6) established that the optimal value for the equivalent geometrical instantaneous strain for soils of various types is ~1.0. When a material element is eroded, its nodes are retained along with their masses and velocities to conserve momentum of the system.

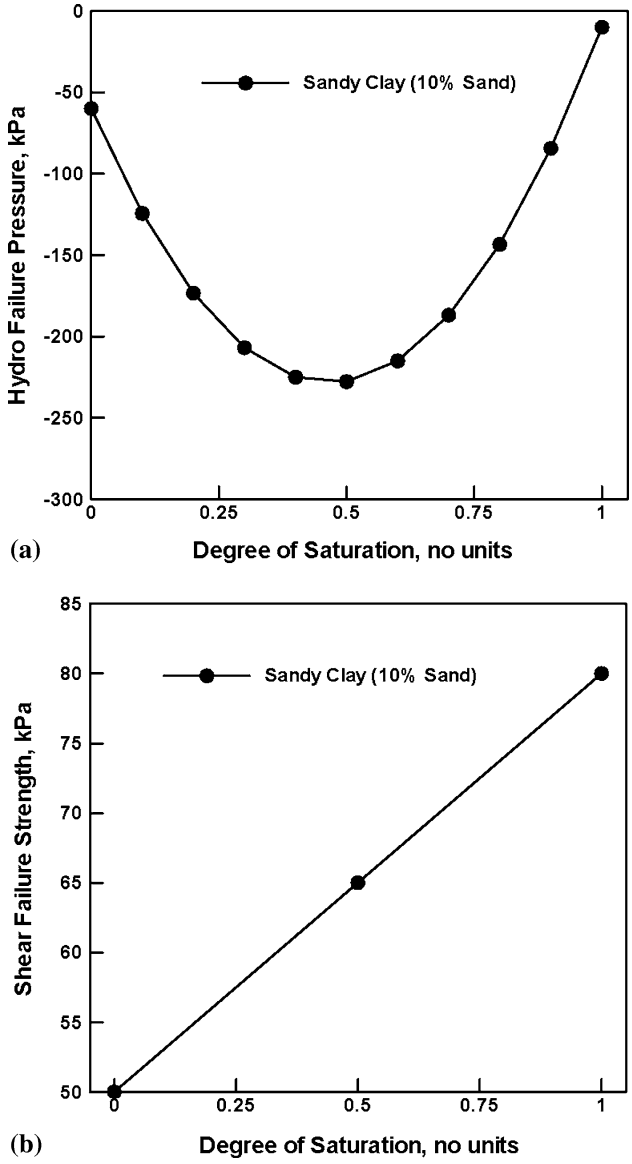

Fig. 5 Variation in (a) hydro failure pressure and (b) shear failure strength for CU-ARL sandy clay (10 vol.% sand) with degrees of saturation

3. Validation of the CU-ARL Sandy-Clay Model

The CU-ARL sandy clay model presented in Sect 2.4 was developed using simple physical arguments regarding the effects of moisture and minor sand contents on the dynamic mechanical behavior of clay-based soils. The model was next parameterized using various soil-testing experimental results and property-correlation analyses. The parameterizations of the CU-ARL sandy clay model for the dry, 50% unsaturated, and saturated sandy clay with 10 vol.% sand are given in Table 1-3. In order to facilitate implementation of these parameterizations into the ANSYS/Autodyn material library, a piece-wise linear representation of the EOS and the strength models were used. In this section, an attempt is made to validate the CU-ARL sandy clay model by comparing the available open-literature field-test results pertaining to the detonation of shallow-buried landmines in sandy clay with their computational counterparts obtained in this study. The latter results were obtained by carrying out a set of the transient non-linear dynamics simulations corresponding to the field tests in question. In order to assess the potential improvements in modeling soil behavior resulting from the use of the CU-ARL sandy clay model, simultaneous non-linear dynamics simulations were also carried out using the original Laine and Sandvik dry-sand compaction model (Ref 14) which is currently the soil material model most widely used in shallow-buried landmine-detonation computational community. All the computational analyses carried in this study were done using the commercial software ANSYS/Autodyn (Ref 7). A brief description of the essential features of a typical transient non-linear dynamics analysis is discussed in the next section.

3.1 The Basics of Transient Non-Linear Dynamics Simulations

A transient non-linear dynamics problem is analyzed within ANSYS/Autodyn (Ref 7) by solving simultaneously the governing partial differential equations for the conservation of momentum, mass, and energy along with the materials constitutive equations and the equations defining the initial and the boundary conditions. The equations mentioned above are solved numerically using a second-order accurate explicit scheme and one of the two basic mathematical approaches, the Lagrange approach and the Euler approach. Within ANSYS/Autodyn (Ref 7), these approaches are referred to as "*processors*". The key difference between the two basic processors is that in the Lagrange processor, the numerical grid is attached to and moves along (and deforms) with the material during calculation while in the Euler processor, the numerical grid is fixed in space, and the material moves through it. In our recent study (Ref 5), a brief discussion was given of how the governing differential equations and the materials constitutive models define a self-consistent system of equations for the

Table 1 Material model parameters for dry sandy clay with initial porosity of 0.29 and with 10 vol.% sand

Field dependent variables	Units	Piece-wise model relations									
Reference density, $\rho_{s,drySandyclay}$	kg/m^3	2080.5									
Equation of state											
Density, $\rho_{drySandyclay}$	kg/m^3	1468.7	1536.7	1604.7	1672.6	1740.6	1808.6	1876.6	1944.6	2012.5	2080.5
Pressure, $P_{drySandyclay}$	MPa	0	0.0178	0.0355	0.0533	0.0711	0.0889	0.106	0.124	0.146	0.1601
Sound speed, $C_{drySandyclay}$	m/s	859	1214	1466	1663	2280	2842	3278	3637	5606	5629
Strength model											
Yield strength, $\sigma_{y,drySandyclay}$	kPa	55									
Density, $\rho_{drySandyclay}$	kg/m^3	1468.7	1536.7	1604.7	1672.6	1740.6	1808.6	1876.6	1944.6	2012.5	2080.5
Shear modulus, $G_{drySandyclay}$	MPa	991.3	1001	1074	1271	1655.8	2289	3233	4552	6306	8559
*Hybrid hydro/shear failure mode*l											
Hydro failure pressure, $P_{drySandyclay,fail}$	kPa	−60									
Shear failure pressure, $\tau_{drySandyclay,fail}$	kPa	55.56									
Erosion											
Instantaneous geometric strain	…	2.0									

Table 2 Material model parameters for unsaturated sandy clay (50% saturation) with initial porosity of 0.29 and with 10 vol.% sand

Field dependent variables	Units	Piece-wise model relations									
Reference density, $\rho_{s,unsat,Sandyclay}$	kg/m^3	2080.5									
Equation of state											
Density, $\rho_{unsat,Sandyclay}$	kg/m^3	1613.7	1645.7	1677.7	1709.7	1741.7	1773.7	1805.7	1837.7	1869.8	1901.8
Pressure, $P_{unsat,Sandyclay}$	MPa	0	0.0178	0.0355	0.0533	0.0711	0.0889	0.106	0.124	0.146	0.1601
Sound speed, $C_{unsat,Sandyclay}$	m/s	2424.6	2477.4	2526.5	2572.2	2783.5	3022.5	3234.2	3424.3	4594.2	4622.6
Strength model											
Yield strength, $\sigma_{y,unsat,Sandyclay}$	kPa	28									
Density, $\rho_{unsat,Sandyclay}$	kg/m^3	1613.7	1645.7	1677.7	1709.7	1741.7	1773.7	1805.7	1837.7	1869.8	1901.8
Shear modulus, $G_{unsat,Sandyclay}$	MPa	566.67	571.91	608.61	708.24	902.25	1222.1	1699.3	2365.2	3251.3	4389.1
Hybrid hydro/shear failure model											
Hydro failure pressure, $P_{unsat,Sandyclay,fail}$	kPa	−227.22									
Shear failure pressure, $\tau_{unsat,Sandyclay,fail}$	kPa	72.22									
Erosion											
Instantaneous geometric strain	…	2.0									

Table 3 Material model parameters for saturated sandy clay with initial porosity of 0.29 and with 10 vol.% sand

Field dependent variables	Units	Piece-wise model relations									
Reference density, $\rho_{s,satSandyclay}$	kg/m^3	2080.5									
Equation of state											
Density, $\rho_{satSandyclay}$	kg/m^3	1758.7	1760.5	1762.2	1764	1765.7	1767.5	1769.2	1770.9	1772.7	1774.4
Pressure, $P_{satSandyclay}$	MPa	0	0.0178	0.0355	0.0533	0.0711	0.0889	0.106	0.124	0.146	0.1601
Sound speed, $C_{satSandyclay}$	m/s	3189.2	3189.2	3189.2	3189.2	3189.2	3189.2	3189.2	3189.2	3189.2	3189.2
Strength model											
Yield strength, $\sigma_{y,satSandyclay}$	kPa	0.556									
Density, $\rho_{satSandyclay}$	kg/m^3	1758.7	1760.5	1762.2	1764	1765.7	1767.5	1769.2	1770.9	1772.7	1774.4
Shear modulus, $G_{satSandyclay}$	MPa	133.33	133.33	133.33	133.33	133.33	133.33	133.33	133.33	133.33	133.33
Hybrid hydro/shear failure model											
Hydro failure pressure, $P_{satSandyclay,fail}$	kPa	−10									
Shear failure pressure, $\tau_{satSandyclay,fail}$	kPa	88.89									
Erosion											
Instantaneous geometric strain	…	2.0									

dependent variables (nodal displacements, nodal velocities, cell material densities, and cell internal energy densities).

In this study, both the Lagrange and Euler processors are used. The Lagrange processor was used to model the sand and various targets and structural components. High-energy explosives, gaseous mine-detonation products, and the surrounding air are modeled using either a single-material FCT (Flux Corrected Transport) or a multi-material Euler processor. Different regions of the mine/air/target/sand model are allowed to interact and self-interact using the ANSYS/Autodyn (Ref 7)

interaction options. A brief overview of the parts interactions and self-interaction ANSYS/Autodyn algorithms can be found in our recent study (Ref 5). Also a detailed description of the Lagrange, Euler-FCT, and multi-material Euler processors as well as of the material models used for air, high explosives, and metallic structural materials can be found in our recent study (Ref 4, 5).

Throughout this article, the terms the "*Depth of Burial*" (DOB) and the "*Stand-off Distance*" (SOD), are used to denote distances between the mine top face and the sandy clay/air interface, and between the sandy clay/air interface and the bottom face of the target structure, respectively.

In the next section, a comparison between the computational and experimental results is presented for the spatial and temporal evolution of the sandy clay overburden bubble and the associated pressure fields. Then, a comparison is made between the computational results regarding the total impulse captured by a witness plate obtained using the Laine and Sandvik dry-sand compaction model (Ref 14) and the present CU-ARL sandy clay model.

3.2 Spatial and Temporal Evolution of Soil Overburden Bubble and Pressure Fields

While a number of field-test studies of the detonation of landmines shallow-buried in sand-based soils exist in literature (Ref 9-11, 13), the authors of this article were able to locate only one public-domain source of field-test data pertaining to the landmine detonation associated with clay-based soils (Ref 36). Hence, the validation of the current CU-ARL sandy clay model will be done by comparing the experimental results obtained in Ref 36 with the corresponding computational results obtained in this study. In this section, a brief overview of the experimental set-up and the procedure used in Ref 36 are first presented.

The experiments carried out in Ref 36 can be briefly described as follows: A 1.27-cm wall thickness cylindrical barrel with the outer-diameter of 81.6 cm and the overall height of 71 cm is filled with a clay-based soil up to its top. A 100-g cylindrical-disk shaped C4 high-energy explosive (6.4 cm in diameter and 2 cm in height) is buried into the clay-based soil along the centerline of the barrel with its faces parallel with the clay-based soil surface. A photograph of the experimental setup used in Ref 36 is given in Fig. 6. The Depth of Burial (DOB) (defined as the vertical distance between the top face of the explosive and the clay-based soil surface) is varied in a range between 0 and 8 cm. Thus a zero-centimeter DOB case corresponds to a flush-buried explosive. A set of six pressure transducers is utilized to monitor the pressure in the air following the detonation of the explosive. The designations and the position coordinates of the six transducers are given in Table 4. The first number in the Pressure Transducer (PT) designation represents the distance in centimeters of the transducer from the origin of the coordinate system (defined below), while the second number represents the angular relation in degrees between the position vector of the pressure transducer and the axis of symmetry. The locations of the six pressure transducers is also shown in Fig. 7. In order to be consistent with the definition of coordinate system for the 2D axi-symmetric problem used in ANSYS/Autodyn (Ref 7), the y coordinates are measured in the radial direction from the centerline of the barrel, while the x coordinates are measured along the axis of symmetry, with $x = 0$ corresponding to the sand surface and $x < 0$ denoting the air region above the ground.

Fig. 6 A photograph of the experimental setup used in Ref 36 to study the effect of explosion of a shallow-buried mine

Table 4 Coordinates of the pressure transducers located in air

Transducer designation	Transducer coordinates, cm	
	X	*Y*
PT_30_0	−30.00	0
PT_30_22.5	−27.71	11.48
PT_30_45	−21.21	21.21
PT_70_0	−70.00	0
PT_70_30	−60.62	35.00
PT_110_0	−110.00	0

The origin of the coordinate system is located along the line of symmetry at the sandy-clay/air interface

The physical model displayed in Fig. 7 has been represented using the computational multi-material Euler model shown in Fig. 8. In Fig. 8, various portions of the computational domain are filled with one or more of the attendant materials (air, clay-based soil, C4 gaseous-detonation products, and AISI 1006 mild steel). Due to the inherent axial symmetry of the set-up used in Ref 36, the mine detonation is analyzed as a 2D axi-symmetric problem. The left boundary in Fig. 8 coincides with the axis of symmetry (x-axis). The horizontal direction (y-axis) corresponds to the radial direction.

The "*flow-out*" boundary conditions are applied to all the outer boundaries of the computational domain. In other words, the material at the outer boundary of the domain with a non-zero normal-outward component of the velocity is allowed to leave the computational domain. In order to mimic the detonation initiation conditions used in Ref 36, detonation is

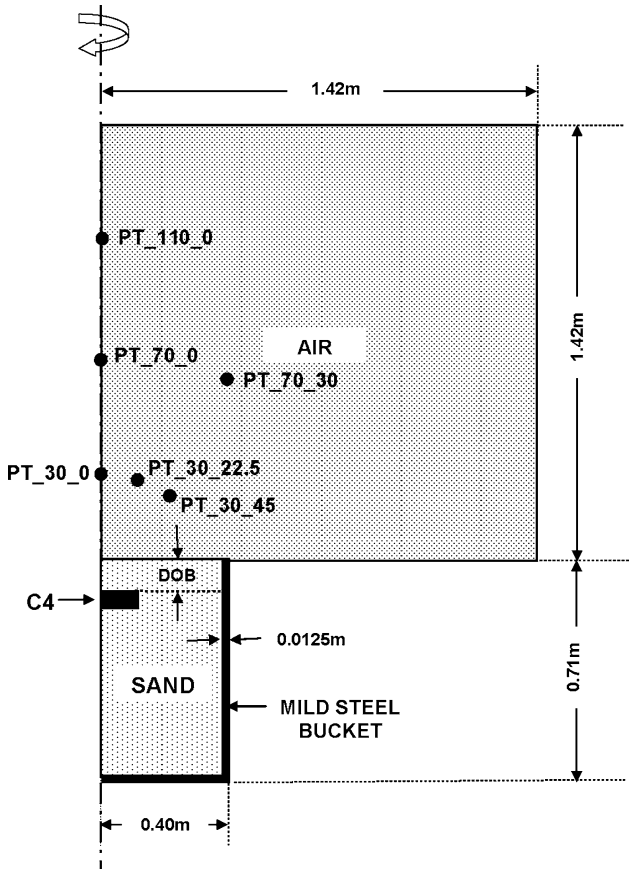

Fig. 7 A simple schematic of the experimental setup used in Ref 36 to study the effect of explosion of shallow-buried mine

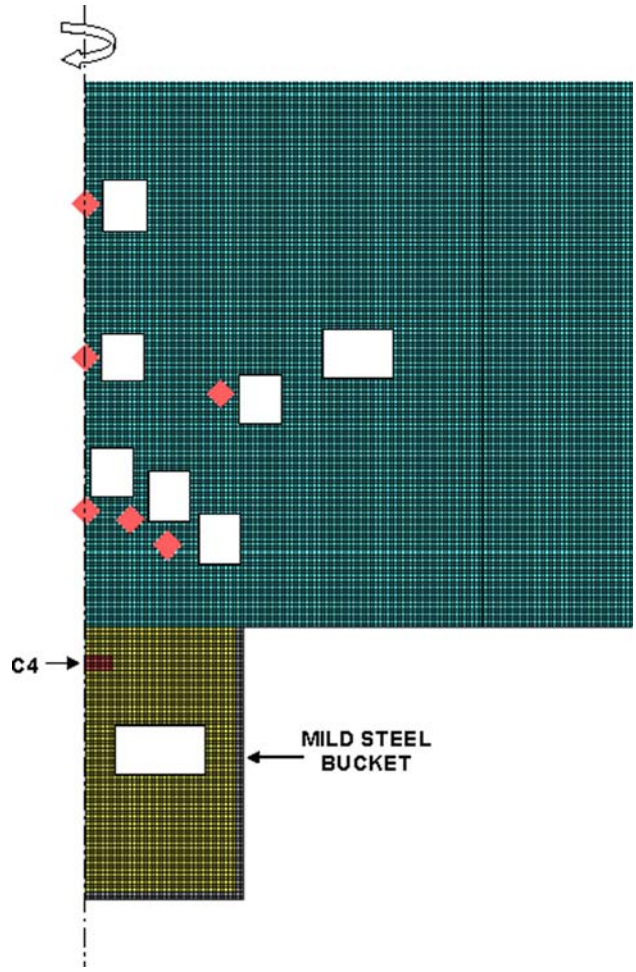

Fig. 8 Computation sub-domains representing the experimental setup used in Ref 36 to study the effect of explosion of a shallow-buried mine

initiated at the central circular portion of the explosive of radius 3.2 cm, at the bottom face of the mine. In order to monitor the temporal evolution of pressure in air, six gage points are introduced whose locations coincide with those of the pressure transducers used in Ref 36.

A standard mesh sensitivity analysis was carried out (the results not shown for brevity) in order to ensure that the results obtained are insensitive to the size of the cells used.

A comparison between the computational results obtained in this study (using the Laine and Sandvik sand model (Ref 14) and the present CU-ARL sandy clay model) and their experimental counterparts (Ref 36) for the cases of dry and saturated clay-based soil is displayed in Fig. 9(a)-(d) and 10(a)-(d), respectively. The results pertaining to the dry sandy clay will be discussed first.

3.2.1 Dry Sandy Clay. The variation of the peak side-on (static) pressure in air with the distance (along the vertical axis) from the sandy-clay/air interface at two (3 and 8 cm) DOBs is displayed in Fig. 9(a). The results displayed in Fig. 9(a) show that at 8-cm DOB, the two models account reasonably well for the observed experimental results. At 3-cm DOB, on the other hand, the Laine and Sandvik model (Ref 14) greatly underpredicts the side-on pressure, particularly at short distances of the pressure transducer from the Sandy-Clay/Air interface. What is even more troubling in the case of the Laine and Sandvik model (Ref 14) is that, in contrast to the experimental findings (Ref 36), it predicts lower values of side-on pressure at 3-cm DOB at the lower values of pressure-transducer distance from sandy-clay/air interface.

The variation of the blast-wave time of arrival with the distance from the sandy-clay/air interface at the same two DOBs is displayed in Fig. 9(b). The results displayed in Fig. 9(b) reveal that, as in the case of Fig. 9(a), the two sets of computational results are in good agreement with the experimental results in the 8-cm DOB case. On the other hand, at 3-cm DOB, the present CU-ARL sandy clay model continues to agree well with the experiments while the Laine and Sandvik (Ref 14) falls short, particularly at larger pressure-transducer distances from the sandy-clay/air interface.

The variation in the blast-wave time of arrival with offset angle (from vertical axis) at a fixed (30 cm) distance from the sandy-clay/air interface is displayed in Fig. 9(c). The results displayed in this figure show that the two models yield reasonably good agreement with the experiment in the case of 3-cm DOB (not 8-cm DOB), while in the case of 8-cm DOB the CU-ARL sandy clay model clearly outperforms the Laine and Sandvik model (Ref 14).

The temporal evolution of the sandy clay bubble height for the cases of 3- and 8-cm DOBs is displayed in Fig. 9(d). The results displayed in this figure show that the Laine and Sandvik model (Ref 14) causes the sand bubble to burst earlier causing the venting of the detonation products in both the 3- and 8-cm DOB cases. The CU-ARL sandy clay model on the other hand,

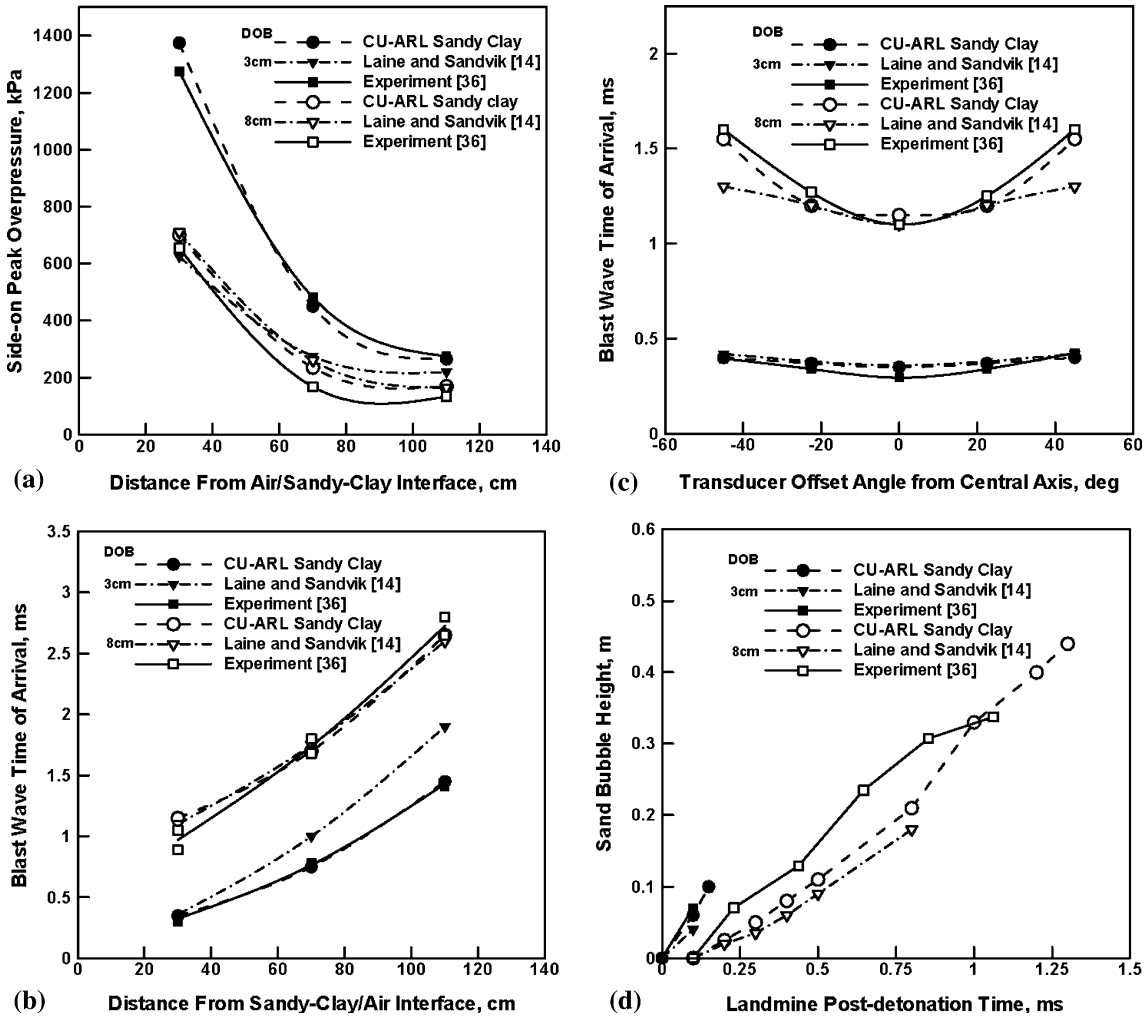

Fig. 9 A comparison of the experimental (Ref 36) and computed (present study) results pertaining to various phenomena associated with landmine detonation in dry sand clay: (a) side-on overpressure vs. transducer distance from air/sandy clay interface, (b) blast wave arrival time vs. transducer distance from air/sandy clay interface, (c) blast wave arrival time vs. transducer offset angle from the symmetry axis and (d) sand clay bubble height vs. landmine post-detonation time

predicts substantially higher values of sand-bubble height at the moment of venting. Additional computations carried out in this study revealed that this short-coming of the CU-ARL sandy clay model can be readily eliminated by small adjustments to the hydrodynamic failure parameters.

3.2.2 Saturated Sandy Clay. A comparison between the computational results and their experimental counterparts in the case of saturated sandy clay is presented in Fig. 10(a)-(d) and discussed below.

The results displayed in Fig. 10(a) show that while both models yield reasonably good agreement with the experiment at 8-cm DOB, the agreement being somewhat better in the case of the CU-ARL sandy clay model. In the case of 3-cm DOB, the CU-ARL sandy clay model clearly outperforms the Laine and Sandvik model (Ref 14) at high values of the pressure-transducer distance from the sandy clay/air interface. However, at low values of this distance, where the Laine and Sandvik model (Ref 14) underpredicts the side-on peak overpressure, the CU-ARL sandy clay model yields higher values of this quantity. Unfortunately, this correction is too excessive making the agreement between the CU-ARL sandy clay model and the experiment less satisfactory.

The variation of the blast-wave time of arrival with the distance from the sandy clay/air interface at the same two DOBs is displayed in Fig. 10(b). A simple analysis of the results displayed in this figure reveals that, at 8-cm DOB, the CU-ARL sandy clay model does not significantly improve the agreement with the experiment and that both models reveal reasonable agreement with the experiment. However, a clear evidence of the improved agreement with the experiment (Ref 36) brought about by the present CU-ARL sandy-clay model is seen in the case of 3-cm DOB.

The variation in the blast-wave time of arrival with offset angle (from vertical axis) at a fixed (30 cm) distance from the sandy clay/air interface is displayed in Fig. 10(c). The results displayed in this figure show that at both 3- and 8-cm DOBs, the agreement between the model predictions is reasonably good, and that the CU-ARL sandy clay model clearly outperforms Laine and Sandvik model (Ref 14).

The temporal evolution of the sandy clay bubble height for the cases of 3- and 8-cm DOBs is displayed in Fig. 10(d). The results displayed in this figure show that the Laine and Sandvik model (Ref 14) clearly underpredicts the maximum value of sand-bubble height (the height when bubble bursting takes

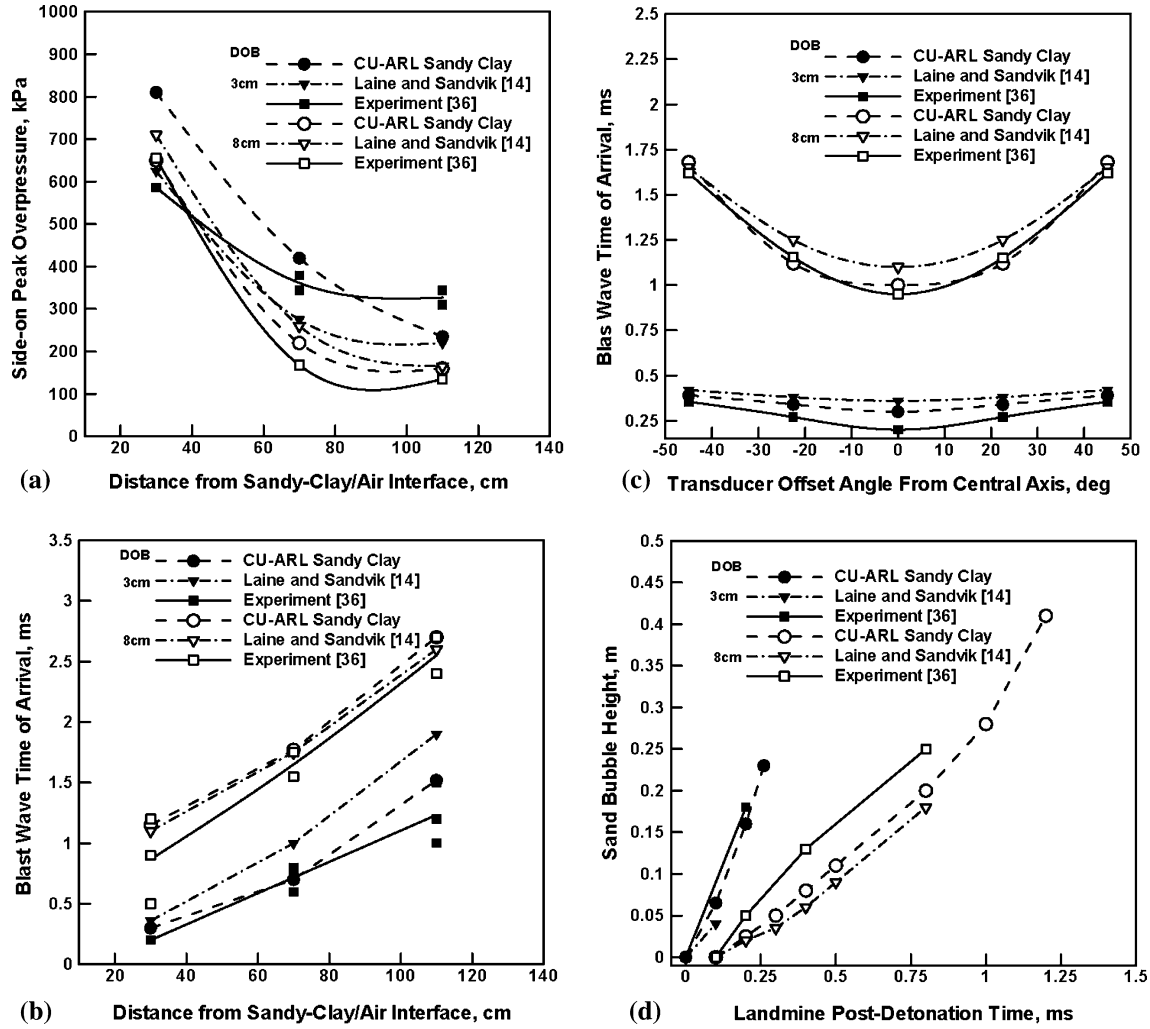

Fig. 10 A comparison of the experimental (Ref 36) and computed (present study) results pertaining to various phenomena associated with landmine detonation in fully saturated sandy clay: (a) side-on overpressure vs. transducer distance from air/sandy clay interface, (b) blast wave arrival time vs. transducer distance from air/sandy clay interface, (c) blast wave arrival time vs. transducer offset angle from the symmetry axis and (d) sand clay bubble height vs. landmine post-detonation time

place), while, the current CU-ARL sandy clay model overpredicts the same. As discussed earlier, this short-coming of the present CU-ARL sandy clay model can be eliminated by small adjustments in the hydrodynamic failure parameters.

Overall, it is found that, in the case of dry and saturated sandy clay, significant improvements in model/experiment agreement are obtained when the widely used Laine and Sandvik sand model (Ref 14) is substituted with the present CU-ARL sandy clay model.

3.3 Total Momentum Transferred to the Target Structure

In order to assess the ability of the CU-ARL sandy clay model to account for the total momentum transferred to the target structure following detonation of a ground-laid or shallow-buried mine at different soil saturation levels, a set of experimental field-tests is planned to be conducted in the near future. A Vertical Impulse Measurement Fixture (VIMF) will be used. The experimental test matrix to be used is displayed in Table 5 and the results to be obtained will be compared with their computational counterparts. In this section, in the absence of the experimental results, a comparison will be made between the computational results obtained using the Laine and Sandvik sand model (Ref 14) and the present CU-ARL sandy clay model. It is often found that the Laine and Sandvik sand model

Table 5 Computed impulse (N-s) transferred to the VIMF witness plate for the case of cylindrical disc-shaped TNT charge (diameter = 0.254 m, height = 0.056 m and mass = 4.540 kg)

DOB, cm	SOD, cm	Laine and Sandvik sand model, N s	CU-ARL sandy clay model, N s
Dry clay-based soil			
3	20	15100	22100
8	20	18600	26200
3	40	11550	14200
8	40	13270	20750
Saturated clay-based soil			
3	20	15100	30700
8	20	18600	35470
3	40	11550	21100
8	40	13270	28750

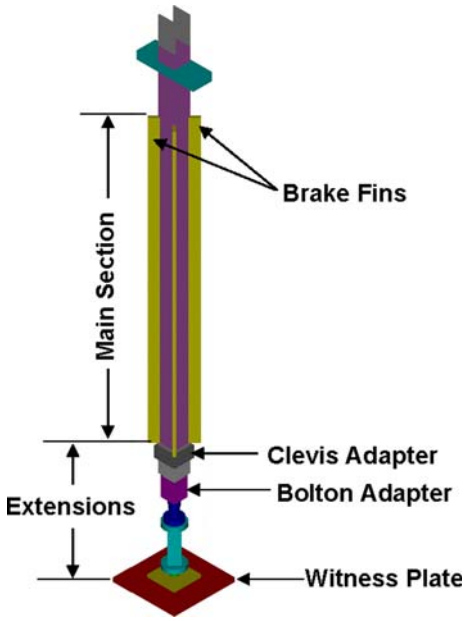

Fig. 11 The vertical impulse measurement fixture (VIMF)

underpredicts the total momentum transferred to the target structure (e.g. Ref 5). Hence, it is interesting to learn whether the present CU-ARL sandy clay model predicts higher values of this momentum.

The VIMF, Fig. 11, is a structural mechanical device that enables direct experimental determination of the imparted blast-loading impulse via measurements of the vertical displacement of a known fixed-mass vertical guide rail that is capped with a witness plate, which serves as a momentum trap to capture the blast loading of the buried charge. The design and operation of the VIMF has been described in details by Taylor et al. (Ref 37), Gniazdowski (Ref 38), and Skaggs et al. (Ref 39) and will be only briefly discussed here. In order to create the required water-saturated soil condition, a cylindrical pit, 3.65 m in diameter and 1.32 m deep is first constructed in the soil within the VIMF test area. In order to retain water in the soil pit and to keep the soil-water mixture separated from the rest of the soil, the walls of the pit are lined with 0.32-cm-thick poly-ethylene sheets, and the pit floor is built using a commercial swimming pool liner. Once the pit liners are in place, a series of water hoses is placed in pit bottom to allow the introduction of water into the pit from the bottom. Next, approximately, 14.2 m^3 of soil is placed in the pit. The soil to be used in the planned experimental field tests and also used in the present computational study is clay-based and contains 10 vol.% sand. In the case of saturated soil, water is allowed to fill the soil pit until standing water is observed on top of the soil.

The basic formulation of the computational problem dealing with the interactions between the detonation products, shell fragments, and soil ejecta (all resulting from the explosion of a shallow-buried landmine) and the VIMF are presented next. The computational modeling of this interaction involved two distinct steps: (a) geometrical modeling of the VIMF along with the adjoining mine, air, and soil regions, and (b) the associated transient non-linear dynamics analysis of the impulse loading (momentum transfer) from the detonation products, shell fragments, and soil ejecta to the VIMF structure. The part (b) of this analysis was performed using a modified version of the

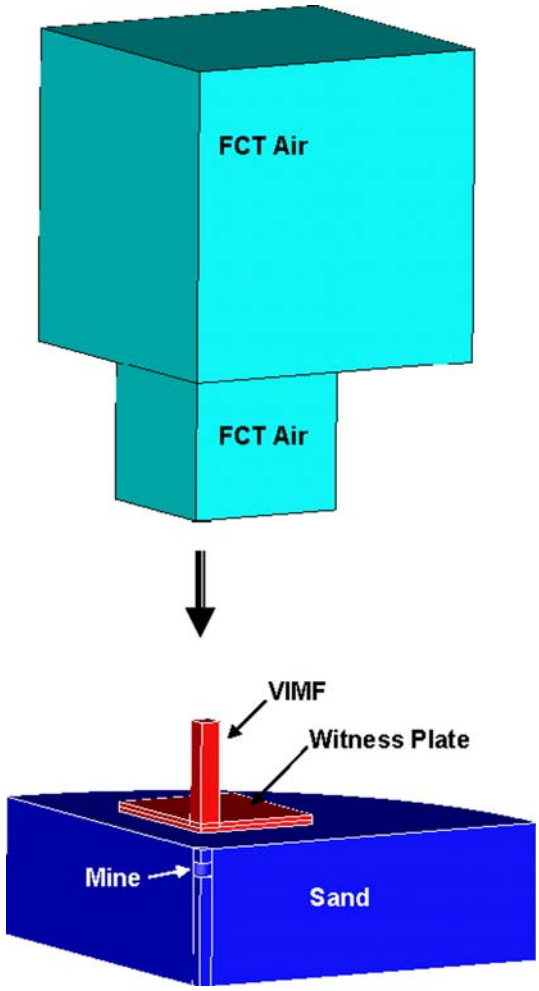

Fig. 12 Computational sub-domains used in this study

technique developed by Fairlie and Bergeron (Ref 40). This technique couples a multi-material Eulerian mesh to three Lagrangian meshes. The Eulerian mesh contained initially a TNT mine (and after mine explosion the resulting high-pressure, high-internal energy-density detonation products) and the (initially stationary, atmospheric-pressure) air. The mesh was constructed in terms of eight node elements. One of the Lagrangian mesh was used to model the soil, the other to represent the VIMF witness plate, while the third one was used to model the remainder of the VIMF structure. The soil and the VIMF structure were modeled using eight node solid elements, while the witness plate was modeled using four-node shell elements.

An advantage was taken of the inherent symmetry of the model. In other words, two mutually orthogonal vertical planes of symmetry were placed along the axis of the VIMF as well as along the axis of the air, mine, and sand regions which enabled only a quarter of the computational model to be analyzed. Representative models for various computational domains used in the present study are shown in Fig. 12. It should be noted that the lower portion of the Eulerian domain contains partly the landmine, while the rest of the lower portion of the Eulerian domain is occupied by the Lagrangian soil mesh. Similarly, the upper portion of the Eulerian domain which extends above the soil contains initially air and is partially occupied by the Lagrangian VIMF witness-plate and vertical-base meshes.

At the beginning of the simulation, all the Lagrange and Euler domains were activated and the landmine detonated. The (circular-disk shape) mine was detonated over its entire bottom face at the beginning of the simulation.

A standard mesh sensitivity analysis was carried out (the results not shown for the state of brevity) to ensure that the results obtained are insensitive to the size of the cells used.

A comparison between the two sets of computational results (one based on the use of the Laine and Sandvik sand model and the other based on the use of the present CU-ARL sandy clay model) pertaining to the total impulse transferred to the VIMF is shown in Table 5. The two cases of the DOB (3 and 8 cm) and two cases of stand-off distance (20 and 40 cm) for both dry and saturated clay-based soils are considered. The results displayed in Table 5 suggest that the present CU-ARL sandy clay model predicts the total impulse values which, in the case of dry soil, are on average 30-50% higher than their counterparts obtained using the Laine and Sandvik sand model (Ref 14). This increase is as high as 100% in the case of saturated soil. These findings are quite encouraging suggesting that the present model should also remove some of shortcomings of the Laine and Sandvik sand model (Ref 14) with respect to the ability to predict computationally the correct level of the total impulse transferred to a target structure.

4. Summary and Conclusions

Based on the results obtained in this study, the following main summary remarks and conclusions can be drawn:

1. Based on a simple procedure including physical arguments and a property correlation analysis, a new material model for clay-based soils named CU-ARL sandy clay model has been developed and parameterized.
2. The resulting CU-ARL sandy clay model was validated by comparing the model predictions with their experimental counterparts for a number of scenarious involving detonation of a landmine (buried in sand) and the interactions of the mine fragments, detonation products, and sand ejecta with various target structures.
3. The comparison between the experimental and the computational results (those based on the Laine and Sandvik sand model (Ref 14) and the CU-ARL sand clay model) revealed that the CU-ARL sandy clay model shows significantly better agreement with the experiment.

Acknowledgments

This study is based on the support provided by the U.S. Army/Clemson University Cooperative Agreements, W911NF-04-2-0024 and W911NF-06-2-0042, and by the U.S. Army Grant Number DAAD19-01-1-0661, and through an ARC-TARDEC research contract.

References

1. J. Heffernan, *Pentagon Announces Specific Plans to Use Mines in Iraq*, http://www.banminesusa.org/news/946_pentagon.htm, March 2003
2. M.P.M. Rhijnsburger, Overview of the Use of LS-Dyna in Close-in Explosive Problems at TNO-PML, *11th International Symposium on Interaction of Effects of Munitions with Structures*, Manheim, Germany, May 2003
3. Centers for Disease Control (CDC), Landmine Related Injuries, *Morb. Mortal. Wkly. Rep.*, 1997, **46**, p 724–726
4. M. Grujicic, B. Pandurangan, and B. Cheeseman, The Effect of Degree of Saturation of Sand on Detonation Phenomena Associated with Shallow-Buried and Ground-Laid Mines, *Shock Vib.*, 2006, **13**, p 41–61
5. M. Grujicic, B. Pandurangan, N. Coutris, B.A. Cheeseman, W.N. Roy, and R.R. Skaggs, Derivation and Validation of a Material Model for Clayey Sand for Use in Landmine Detonation Computational Analysis, *Multidiscipline Modeling Mater. Struct.*, accepted for publication, May 2007
6. M. Grujicic, B. Pandurangan, N. Coutris, B.A. Cheeseman, W.N. Roy, and R.R. Skaggs, Computer-Simulations Based Development of a High Strain-Rate, Large-Deformation, High-Pressure Material Model for STANAG 4569 Sandy Gravel, *Soil Dyn. Earthq. Eng.*, accepted for publication, December 2007
7. *ANSYS/Autodyn-2D and 3D, Version 11, User Documentation*, Ansys Inc., 2007
8. K.A. Holsapple and K.R. Housen, *Crater Database and Scaling Tools*, http://keith.aa.washinton.edu/craterdata, November 2004
9. P.S. Westine, B.L. Morris, P.A. Cox, and E. Polch, *Development of Computer Program for Floor Plate Response from Landmine Explosions*, Contract Report No. 1345, for U.S. Army TACOM Research and Development Center, 1985
10. B.L. Morris, *Analysis of Improved Crew Survivability in Light Vehicles Subjected to Mine Blast*, Final Report for Contract No. DAAK70-92-C-0058 for the U.S. Army Belvoir RDEC, Ft. Belvoir, VA, 1993
11. D. Bergeron, S. Hlady, and M.P. Braid, Pendulum Techniques to Measure Landmine Blast Loading, *17th International MABS Symposium*, Las Vegas, USA, June 2002
12. M. Grujicic, B. Pandurangan, and B. Cheeseman, A Computational Analysis of Detonation of Buried Mines, *Multidiscipline Modeling Mater. Struct.*, 2006, **2**, p 363–387
13. D. Bergeron, R. Walker, and C. Coffey, *Detonation of 100-gram Anti-Personnel Mine Surrogate Charges in Sand-A Test Case for Computer Code Validation*, Suffield Report No. 668, Defence Research Establishment Suffield, Ralston, Alberta, Canada, April 1998
14. P. Laine and A. Sandvik, Derivation of Mechanical Properties for Sand, *Proceedings of the 4th Asia-Pacific Conference on Shock and Impact Loads on Structures*, CI-Premier PTE LTD, Singapore, November 2001, p 361–368
15. D. Bergeron and J.E. Tremblay, Canadian Research to Characterize Mine Blast Output, *16th International MABS Symposium*, Oxford, UK, September 2000
16. M. Grujicic, B. Pandurangan, B.A. Cheeseman, W.N. Roy, and R.R. Skaggs, Impulse Loading Resulting from Shallow Buried Explosives in Water-saturated Sand, *J. Mater. Design Appl.*, 2007, **221**, p 21–35
17. A.M. Bragov, A.K. Lomunov, I.V. Sergeichev, K. Tsembelis, and W.G. Proud, The Determination of Physicomechanical Properties of Soft Soils from Medium to High Strain Rates, in process of submission, November 2005
18. D.J. Chapman, K. Tsembelis, and W.G. Proud, The Behavior of Water Saturated Sand Under Shock-Loading, *Proceedings of the 2006 SEM Annual Conference and Exposition on Experimental and Applied Mechanics*, 2006, Vol. 2, p 834–840
19. M. Grujicic, B. Pandurangan, B.A. Cheeseman, W.N. Roy, R.R. Skaggs, and R. Gupta, Parameterization of the Porous-Material Model for Sand with Various Degrees of Water Saturation, *Soil Dyn. Earthq. Eng.*, 2008, **28**, p 20–35
20. STANAG 4569- *Protection Levels for Occupants of Logistics and Light Armored Vehicles*
21. G. Eisenstadt and D. Sims, Evaluating Sand and Clay Models: Do Rheological Differences Matter?, *J. Struct. Geol.*, 2005, **27**, p 1399–1412
22. J. Henrych, *The Dynamics of Explosion and Its Use, Chapter 5*, Elsevier Publications, New York, USA, 1979
23. B. Loret and N. Khalili, A Three-Phase Model for Unsaturated Soils, *Int. J. Numer. Anal. Meth. Geomech.*, 2000, **24**, p 893–927
24. Z. Wang, H. Hao, and Y. Lu, A Three-phase Soil Model for Simulating Stress Wave Propagation Due to Blast Loading, *Int. J. Numer. Anal. Meth. Geomech.*, 2004, **28**, p 33–56

25. A. Revil, D. Grauls, and O. Brevart, Mechanical Compaction of Sand.Clay Mixtures, *J. Geophys. Res.*, 2002, **107**(B11), p 1–15, ECV 11
26. Y.M. Tien, P.L. Wu, W.S. Chuang, and L.H. Wu, Micromechanical Model for Compaction of Bentonite-Sand Mixtures, *Appl. Clay Sci.*, 2004, **26**, p 489–498
27. M.W. Lee, Geophysical Prospecting of the Biot Coefficient in Predicting Shear-Wave Velocity in Water-Saturated Sediments, *Geophys. Prospect.*, 2006, **54**, p 177–185
28. L. Laine, Numerical Simulation of Ground Shock Attenuation Layer for Swedish Rescue Centers and Shelters, *Proceedings of the 4th Asia Pacific Conference on Shock and Impact Loads on Structures*, 2001, p 1–8
29. S.R. Cohen, "Measurement of Visco-Elastic Properties of Water-Saturated Clay Sediments," Master's thesis, Naval Postgraduate School, Monterey, CA, 1968
30. A. Sanna and D. Penumadu, Shear Modulus and Damping Variation During Consolidation of Clay, Project Report, *SURE Symposium*, Clarkston University, 2000
31. S. Stein and T. Kim, Effect of Moisture on Attraction Force on Beach Sand, *Mar. Geosour. Geotechnol.*, 2004, **22**, p 33–47
32. S.N. Abduljauwad and H. Rehman, Effect of Oil Contamination on the Behavior of Calcareous Expansive Clays, *Proceedings of the 12th Southeast Asian Geotechnical Conference*, Malaysia, 1996, Vol. 1, p 505–510
33. N.A. Al-Shayea, The Combined Effect of Clay and Moisture Content on the Behavior of Remolded Unsaturated Soils, *Eng. Geol.*, 2001, **62**, p 391–342
34. J. Kuwano, Y. Yoshida, and K. Ishihara, Change in the Stability of Slopes with Degree of Saturation, *Fifth Australia-New Zealand Conference on Geomechanics, National Conference Publication*, Institution of Engineers, Australia, 1988, Vol. 88/11, p 465–469
35. G.G. Moses and S.N. Rao, Behavior of Marine Clay Subjected to Cyclic Loading with Sustained Shear Stresses, *Mar. Geosour. Geotechnol.*, 2007, **25**, p 81–96
36. J. Foedinger, Methodology for Improved Characterization of Landmine Explosions, *SBIR Phase-II Plus Program, Technical Interchange Meeting*, Material Science Corporation, June 2005
37. L.C. Taylor, R.R. Skaggs, and W. Gault, Vertical Impulse Measurements of Mines Buried in Saturated Sand, *Fragblast*, 2005, **9**(1), p 19–28
38. N. Gniazdowski, *The Vertical Impulse Measurement Facility Maintenance and Inspection Manual,* ARL Technical Report (in submission) 2004
39. R.R. Skaggs, J. Watson, T. Adkins, W. Gault, A. Canami, and A.D. Gupta, *Blast Loading Measurements by the Vertical Impulse Measurement Fixture (VIMF)*, ARL Technical Report (in submission)
40. G. Fairlie and D. Bergeron, Numerical Simulation of Mine Blast Loading on Structures, *Proceedings of the 17th Military Aspects of Blast Symposium*, Nevada, June 2002